# Accepted Manuscript

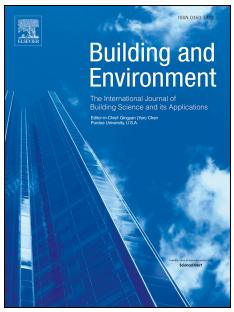


Design and validation of a compact embedded photometric device for real-time daylighting computing in office buildings

Yujie Wu, Jérôme H. Kämpf, Jean-Louis Scartezzini

PII: S0360-1323(18)30711-X

DOI: https://doi.org/10.1016/j.buildenv.2018.11.016

Reference: BAE 5809

To appear in: *Building and Environment*

Received Date: 11 September 2018

Revised Date: 9 November 2018

Accepted Date: 14 November 2018

Please cite this article as: Wu Y, Kämpf JéôH, Scartezzini J-L, Design and validation of a compact embedded photometric device for real-time daylighting computing in office buildings, *Building and Environment* (2018), doi: https://doi.org/10.1016/j.buildenv.2018.11.016.

# Design and Validation of a Compact Embedded Photometric Device for Real-time Daylighting Computing in Office Buildings

Yujie Wu[a,*], Jérôme H. Kämpf[b], Jean-Louis Scartezzini[a]

[a]*Solar Energy and Building Physics Laboratory (LESO-PB), École polytechnique fédérale de Lausanne (EPFL), CH-1015, Lausanne, Switzerland*
[b]*Haute école d'ingénierie et d'architecture Fribourg (HEIA-FR), CH-1705, Fribourg, Switzerland*

**Abstract**

Studies have shown that the exposure to daylight can have substantial visual/non-visual benefits for building occupants. To optimise daylighting provision while maintaining a comfortable visual environment, daylighting control systems have been investigated by architectural design and academic research for a number of years. However, real-time regulation of daylighting in buildings requires transient daylighting simulation with high accuracy and, daylighting simulation, as performed to date, is significantly impacted by the employed sky luminance distribution models which only crudely reproduce the real sky characteristics due to oversimplification and limited luminance sampling inputs.

In this paper, an embedded photometric device is proposed to combine high dynamic range (HDR) imaging based high-resolution sky luminance monitoring with quasi real-time on-board daylighting computing, composed of a low-cost image sensor and a field programmable gate array (FPGA) micro-processor. A deliberate calibration procedure of the whole imaging system, regarding its spectral response (spectral correction error f'1 = 8.89%), vignetting effect and signal response, was formulated and validated experimentally. The device was made to measure a wide luminance range (150 dB) including that of the direct solar disk, sky vault, and landscape simultaneously. Finally, experiments during predominant clear and overcast sky conditions were conducted respectively to assess its performance in daylighting simulation, both qualitatively and quantitatively. The experimental results demonstrated its quality in solar tracking as well as its capability to reduce daylighting simulation error to $\frac{1}{7} \sim \frac{1}{3}$ of that of a common practice using the conventional Perez all-weather sky model for workplane illuminance calculation in office buildings.

*Keywords:* Real-time, Daylighting simulation, FPGA, Embedded photometric system, Solar tracking, Workplane illuminance

## 1. Introduction

While there is an ample consensus on the fact that the global energy consumption is rapidly growing [1, 2], global warming and environmental pollution have in many ways catalysed campaign of energy savings all around the world [3]. Among the many energy consuming domains, the building sector is responsible for a considerable fraction of total consumption [4]. And lighting is one of the leading consumers representing 15%-35% of the energy demand in commercial buildings [5–7], despite of its high electricity saving potential [8–12].

The technology of solid-state lighting (SSL) has improved the energy efficiency and life span of luminaires with enhanced luminous efficacy, and restrictions and norms on inefficient light sources have further promoted the diffusion of these luminaires with energy-efficient electronics [13]. In addition, the recent progress in research and development of smart lighting systems based on an human centric approach [14] as well as Internet of Things (IOT) has further confirmed their energy-saving potential in lighting [15, 16]. Nonetheless, it has been revealed in studies that the daylight, as an ubiquitous cost-economical light source, cannot be fully substituted by the current technology of artificial light, not only due to its unique spectral power distribution [17] but also because of its non-visual effects on occupants' physiology, behaviour and circadian rhythms [18–20], which indirectly influence human's health [21, 22] and performance [23]. Within developed economies, such as in Europe and North America, people spend 90% of their time on activities and environments relying on artificial lighting [24, 25]. Therefore, increasing the daylight provision in buildings has gained growing concerns and interests for building designers and researchers.

As a free available resource, daylight utilization can contradict the energy saving objective, if it were not harnessed smartly. During hot seasons, large solar heat gain induced by excessive penetration of sun light can cause a substantial upsurge in the cooling load of buildings [26]. Although shading systems offer a measure for regulating sunlight influx, the utilization of daylight is largely dependent on occupants' behaviour [27]. Once visual comfort is disturbed by glare due to the penetration of sunlight, occupants tend to be reluctant in re-

*Corresponding author at: Solar Energy and Building Physics Laboratory (LESO-PB), École polytechnique fédérale de Lausanne (EPFL), CH-1015, Lausanne, Switzerland

*Email address:* yujie.wu@epfl.ch (Yujie Wu)

opening the shading [28], even if the disturbance has passed, occluding the daylight.

Several studies have shown that an optimal utilization of daylight can not only contribute to 25%-60% of savings in lighting [9, 29] but can also improve occupants' visual comfort substantially [30, 31]. Since occupants' visual comfort has a positive impact on their productivity [32], the productivity saving, when projected to salaries and benefits, is estimated to be even more significant than energy bills in office buildings [33, 34]. Daylighting simulation is a common way to pre-plan and analyse the daylight utilization in buildings, by using advanced techniques of image rendering and daylighting metrics calculation. Although annual simulation of day-lit intra-scene applications in buildings has shown convincing results [35], if the time scale shrinks to minutes or even seconds especially when daylighting simulation is applied in real-time shading or lighting control, the discrepancy between simulation and reality is significant for transient computation [36], since the simulation is contingent upon simplified sky luminance models. Sky models were formulated for the initial purpose of comparing different sky luminance distributions, including clear, overcast and partly cloudy skies. They are commonly based on the averages of a range of sky types and cannot precisely describe a sky for a specific location and moment in time [37].

The International Commission on Illumination (CIE) has defined 15 different standard sky types [38] including the CIE clear and CIE overcast sky. The luminance distribution of the CIE clear and overcast sky can be regarded as two extremes of naturally occurring skies, and most real skies are intermediate ones between them. To make the modelled sky change dynamically according to the weather, Perez proposed the all-weather sky model [39] based on the solar zenith angle, sky clearness, and the sky brightness, which can be derived from the direct normal and diffused horizontal irradiance. Despite of its dynamic feature according to the sky radiation, the Perez all-weather model is derived from the sky luminance monitored in Berkeley, CA, USA, which does not necessarily cover all the sky conditions for any part of the world [40]. Although the CIE General Standard sky 2003 [41] adopted sky models based on scanned sky luminance at extended locations of Berkeley, Tokyo, and Sydney, the sky model based on empirical formulae and fitted parameters share the same issue and cannot address influence of local micro-climate. Furthermore, reconstructing the real sky would require the sampling frequency at least twice as high as the maximum spatial frequency of the sky luminance map, according the Shannon sampling theorem [42]. In contradiction to this, the Perez all-weather model based on merely two inputs and massive interpolation can hardly reconstruct the real sky with precision at the time scale of minutes or seconds, since cloud edges and high contrast sky patches require a much higher sampling frequency or resolution. In addition, the common practice of modelling the ground with a constant reflectance plane contributes to noticeable disparity with reality since the material of the ground can be diverse: while the snow reflectance can reach 75%, that of the asphalt is around 7%. Moreover, the solar luminance sensed from the ground alters according to the position of the sun and weather conditions including mist, smog and haze. To address these limitations, preliminary investigations based on HDR imaging techniques for sky luminance monitoring [43] have been conducted, pointing out its improved accuracy in sky reproduction.

Recent progress in microelectronics has enabled Complementary Metal Oxide Semiconductor (CMOS) image sensors gradually substitute of Charge-Coupled Device (CCD) image sensors [44], thanks to their better signal-noise ratio (SNR), dynamic range (DR) and data output speed. Among others, CMOS image sensors exhibit advantages in the compatibility with computing circuits, versatility of imaging patterns and low power consumption. Simultaneously, the development of microprocessor technology has set a trend toward smaller size, lower power consumption and massive processing speed [45]. The performance of current micro-processing unit (MPU) has made it possible to couple an MPU and high-resolution image sensors into an embedded platform for data acquisition and real-time processing.

Studies have highlighted the possibility of using such image sensors as a reliable luminance monitoring apparatus. Stumpfl et al. [46] suggested an approach for photo-realistic rendering using a digital single-lens reflex (DSLR) camera by 7 consecutive frames to build-up a 132 dB dynamic range picture to capture the sky luminance distribution. Wüller et al. [47] converted, for photometric purposes, the RGB grey-scale values of images by a DSLR camera into the xyY color space by linear matrix transformation to acquire a luminance value from each pixel. The limitation of this DSLR camera based approach are manifold: i) pixels monitoring the direct solar disk are commonly overexposed, its luminance being not directly measurable, ii) capture of multiple frames employs multiple lens aperture, which adds to difficulty to the calibration process, iii) the image acquisition process is time consuming due to aperture change, and last but not least, iv) the RGB channel response of an image sensor is device dependent and, without an 'adhoc' calibration, a simple linear color space conversion for luminance monitoring is commonly associated with noticeable errors [48]. Borisuit et al. [49] used a high dynamic range (HDR, 132 dB) achromatic B&W camera for luminance mapping of indoor spaces. Two color filters were applied to rectify the spectral response of the camera in order to get close to the photometric sensitivity of humans. Nonetheless, the luminance detection range of such a device is not large enough to cope with the luminosity of the sun and sky, and the HDR image sensors normally sacrifice the resolution for larger pixel sizes on a silicon wafer, whose cost and availability is not a neglectable issue.

In this paper, an embedded photometric device employing a low-cost RGB channel image sensor and a Field-Programmable Gate Array (FPGA) processor was suggested for real-time onboard lighting simulation of an office room based on HDR imaging techniques for sky luminance mapping (Section 2). A calibration procedure appropriate for a low-cost image sensor, in

regards to spectral response, vignetting correction and signal gain curves, was applied in order to be able to simultaneously measure the luminance of the sun disk, the sky vault and landscape (Section 3). Finally, in-situ experiments in a 1:1 scale daylighting test module were carried-out to assess the performance and accuracy of the embedded photometric device for sky luminance mapping and lighting simulation of an office room, compared to a common practice employing the Perez all-weather sky model (Section 4).

## 2. Device Architecture

A highly self-sufficient system is normally comprised of microprocessor units (MPUs), memory, sensors and actuators. In the case of lighting simulation, the computation load for an MPU is formidably heavy in the massive calculation of ray-tracing algorithms [50]. A field programmable gate array (FPGA) chip with system on-chip (SoC) architecture was selected as the major MPU of the platform, due to its high-speed performance in both calculation and input/output (IO) and due to its flexibility in communication with sensors or actuators. In the context of sky luminance monitoring under extreme solar radiation, a low-cost image sensor with high-speed shutter was selected for sensing the whole sky, including the direct sun disk, the sky vault, and clouds. The specification and detailed architecture of the components constituting this device are given here after:

### 2.1. Image sensor

The image sensor is fundamentally an accurate device for the measurement of light intensity as an array of photo-diodes. An 1/2.5 inch low-cost CMOS image sensor was employed as the main sensing unit. The sensor features 5 million pixels (frame size: $2593 \times 1944$), a 12-bits ADC (analog to digital converter) resolution and 38.1 dB SNR (signal to noise ratio). Its short integration period enables it to detect extreme luminance values without any saturation for outdoor applications. In addition, the maximum data transmission rate of the sensor reached $9.6 \times 10^7$ pixels/second to output a full frame in 70 ms. Its 381 mW peak power at maximum resolution satisfies the constrain of low-power consumption applying to the component of an embedded device. Furthermore, the wide range of operation temperature ($-30°C$ *to* $+70°C$) allows its application in most geographical locations on the planet. Regarding the shutter mode, the electronic rolling shutter (ERS) was chosen, ensuring an identical exposure time for each pixel at various positions on the image plane [51]. The pixel array was arranged in the RGB Bayer pattern, as illustrated in Figure 1, which is a common way of arranging RGB pixels. The ratio of the RGB pixel number was 1:2:1 respectively. For the measurement of photometric variables, since the color information was neglected, 4 pixels were grouped as a sensing unit to detect and synthesize the luminance by each unit. The sensor was also equipped with multiple registers for the configuration of its functionalities, including operation mode, driving frequency, readout pattern and etc.

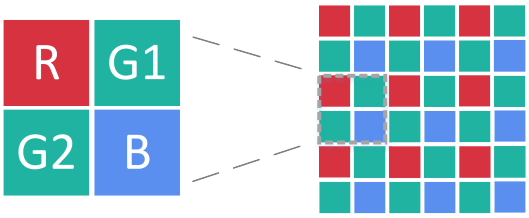


Fig. 1. RGB Bayer pattern of the pixel arrangement of the image sensor

### 2.2. FPGA processor

The FPGA chips have been widely applied by the telecommunication industry, which imposes strict requirements on the data processing and transmission speed [52]. In the context of this paper, its high speed performance matches the demand of bulky data transfer from the image sensor, particularly in case of high dynamic range imaging (HDR), leading to a massive data volume. The recent development of FPGA-SoC architecture, embedding a hard-core-processor (HPS) with FPGA on a single silicon die, has provided further versatility to such processors in operation with high-level algorithms [53]. To balance both performance and compactness, a commercial FGPA chip (Altera Cyclone V) was employed as the main MPU to import bulky pixel data, to control sensor-actuators, and to operate on-board lighting simulation algorithms. This single processor is composed of two major parts: FPGA fabric and HPS. The FPGA fabric part is essentially a massive field of logic blocks (85K logic cells) and a hierarchy of reconfigurable interconnects; each of them can be configured to realize complex logic functions via place-and-route by a hardware description language (HDL). On the field of logic elements, a number of hardware units, including sensor interfaces, memory managing units and calculation accelerators, can be implemented as long as the communication protocol and timing rules are strictly complied with. As shown in Figure 2, a sensor interface was established together with a direct memory access (DMA) unit in the FPGA fabric. The interface was designed with two sub-functionalities: i) control of image sensor, and ii) transfer and pre-processing of pixel data. The image sensor, connected with the processor through bidirectional pins, can be configured by parameters written into an array of registers to set up the frame size, operating mode and shutter type. In addition, the interface also triggers the shutter of the image sensor and regulates the exposure sequences used by the HDR imaging technique during the sky luminance monitoring stage. Then after a frame has been collected on the image sensor, the interface is prepared to read in the pixel data sequentially, to pre-process the data and to arrange it in the external memory through the internal FPGA2SDRAM bridge for further calculation. The HPS part of the processor is an ARM Cortex-A9 (925 MHz) unit with peripherals including SDRAM controllers to access external double data rate three (DDR3) memory and communication bridges with the FPGA fabric part (e.g. HPS2FPGA bridge) to access interfaces and general purpose input/output (GPIO), as shown in Figure 2. A simplified version of Linux has been installed on the ARM unit as operation system configured for embed-

ded devices, where executive programs (including C and C++) can run with relatively high-level algorithms, including luminance mapping and ray-tracing. In this way, the two parts cooperate seamlessly in executing both the low-level algorithms, including data collection, preprocessing and parallel acceleration, and the high-level algorithms, including ray-tracing and Monte-Carlo integration.

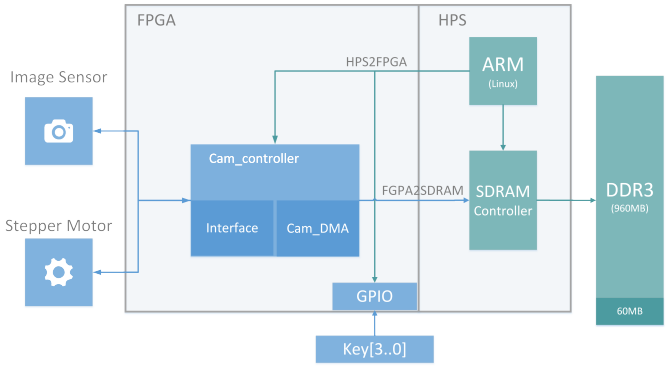


Fig. 2. Modules configured in the FPGA chip and connections with external elements

### 2.3. *Lens and actuator*

To cover both the sky vault and the ground, a wide angle lens with 2.5 mm focal length was coupled with the image sensor as the imaging part of the device. As a super-wide angle lens contributes to noticeable optical distortions in imaging, the field of view (FOV) of the lens was limited to an opening angle of 160° (129.8° × 96.7° in the horizontal and vertical directions respectively), maintaining the distortion at a tolerable level, an image illustrating its FOV is shown in Figure 3. The maximum angular resolution of a pixel is 0.041° (equivalently $5.24 \times 10^{-7}$ *sr* in solid angle), which is one magnitude finer than that of a class B luminance meter (0.33°). The high resolution feature of each pixel makes it possible for the device to detect or even indirectly identify glare sources with particularly minuscule size by simulation.

Fig. 3. Field of view (FOV) of the imaging system

Furthermore, since the device has to be exposed under the sky vault for monitoring, the influence of the direct sun light issued from the solar disk was taken into consideration in the design phase. To mitigate the risk of irreversible physical damage, an opaque shield mask was installed at the front end of the lens to protect the image sensor from overheating under intense solar radiation when the imaging system is idle, as illustrated in Figure 4. A closed-loop stepper motor was also coupled with the shield mask to open and close it when the imaging system performed measurement, keeping the maximum opening time below 0.55 s before the sensor gets overheated.

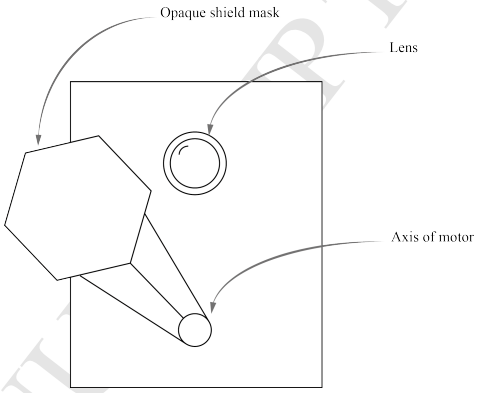


Fig. 4. Protection mask for the imaging system

## 3. Calibration procedure

As the accuracy of lighting computing is contingent on the quality of measurement (sky luminance monitoring), a high quality calibration procedure of the imaging system was formulated, implemented and validated with experiments, including correction of the spectral response, vignetting effect, spatial mapping and response functions.

### 3.1. *Spectral response*

The spectral response of the RGB channels of an image sensor can have pronounced disparity with the color matching function of RGB primaries defined by the standard CIE-1931 triplet stimuli [54]. Its spectral response is commonly device dependent and biased, depending on the manufactures who cater in varying ways to consumers' preference in compelling color. Linear transformation of the response of RGB channels (color space conversion) into the photometric quantity can contribute to substantial errors without optical correction, ignoring the spectral discrepancy, since the photopic luminosity function $V(\lambda)$ normally does not lie in the vector space spanned by $R(\lambda), G(\lambda)$ and $B(\lambda)$, $\lambda$ being the wavelength of incoming radiation. The error tends to be unacceptable particularly when relatively narrow bandwidth light sources are involved [55] in illumination, including light-emitting diode (LED). To address this limitation, the spectral response of the image sensor has been rectified by optical filters. Before selecting the filters, the spectral response of the image sensor with the coupled lens was measured using a spectroradiometer (left, Figure 5) and monochromatic light beams with the experimental set-up shown in Figure 5, of which the diagram is shown in Figure 6. A

monochromator (OMNI-$\lambda$ 300, Zolix), shown on the right side of the figure, was employed to bandpass a narrow bandwidth (20 nm) of light spectrum by the way of a diffraction grating from a high intensity discharge lamp (HID, Xenon arc) used as light source. Since the photometric device dealing with the visual range of the spectrum, the monochromator swept wavelengths of the passing band at 10 nm intervals from 380 nm to 780 nm to cover the entire visual range of the spectrum. An internal near infra-red (NIR) cut-off filter eliminated unnecessary NIR range of the spectrum. In addition, an integration sphere was used to homogeneously diffuse the beam coming from the exit port of the monochromator over the internal surface of the integration sphere. Although the two devices targeted at the same area, the critical role of the integration sphere was to reduce the effect of inevitable misalignment of the FOV of a central pixel on the image plane and that of the spectroradiometer, which showed a different resolution.

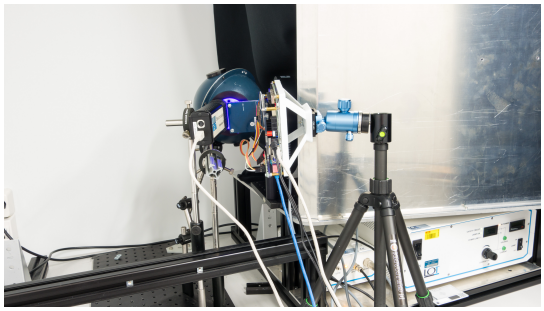

Fig. 5. Set-up of experiments

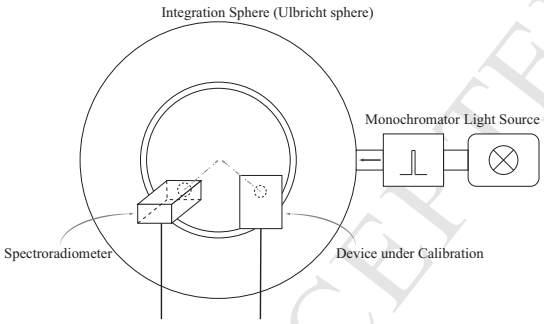


Fig. 6. Diagram of experimental set-up

The experiment was conducted in a darkroom in order to isolate it from parasitic light. Figure 5 and Figure 6 show the photometric device and the spectroradiometer during the calibration; both were fixed at the exit port of an Ulbricht sphere, the input port being aligned with the light beam issued from the monochromator and a light source. After scanning the entire visible spectrum, the pixel response of the image sensor was normalized by the spectral power of the monochromatic light measured by the spectroradiometer (1 nm resolution), leading to the spectral response of each channel illustrated in Figure 7. For each data point, 9 neighbouring pixels at the center of the image plane were averaged for each channel to reduce the spatial noise; the measurement was repeated 5 times to mitigate the temporal noise. Furthermore, the reset noise of pixels was measured and corrected in its response.

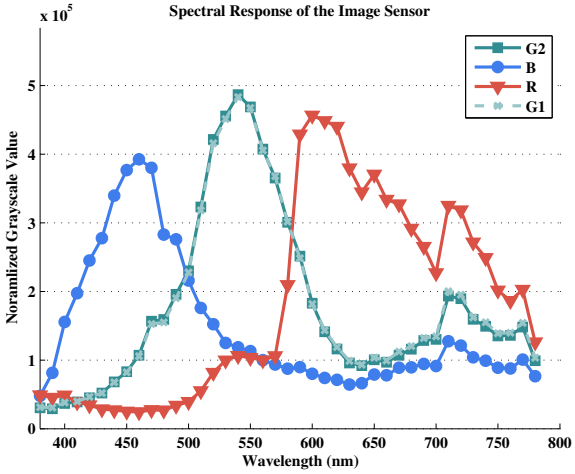


Fig. 7. Spectral response of the RGB channels of the image sensor

As mentioned, to improve accuracy of measuring luminance, the sensor had to be corrected by optical glass filters. The optimization was performed on a pool of bandpass filters (256 models) with neutral-density (ND) filters over 2.8 million combinations to fit the luminosity function $V(\lambda)$, through the least error in the $\ell_2$ norm space. With consideration of the limited space available for filters in imaging system, the optimal set of filters were finally determined using only three filters, a cyan filter, a yellow filter and an ND filter (1% transmittance). The spectral transmittance distribution of the two color filters is presented in Figure 8.

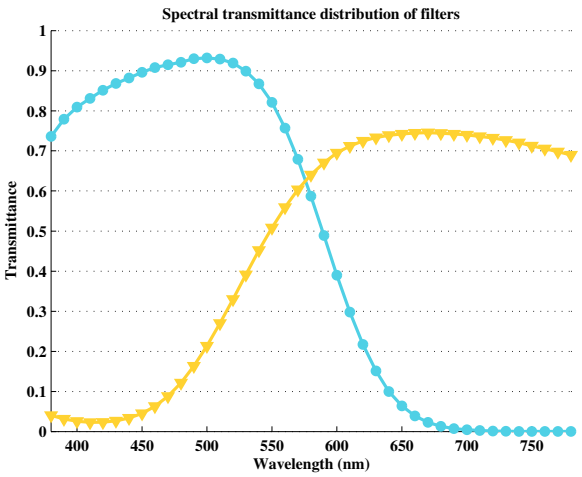


Fig. 8. Spectral transmittance distribution of the color filters

The filters were installed in the imaging system, between the rear side of the lens and the image sensor, instead of in front of the lens, to lessen the mechanical vignetting of the optics. Then the spectral response of the imaging system with embedded filters was measured again with the identical set-up as

Figure 6. To assess the spectral response with high resolution, the center wavelength of the beam was swept at a finer wavelength interval by the monochromator, e.g. every 5 nm from 380 nm to 780 nm. The spatial and temporal noise were again mitigated by averaging 9 center pixels and by repetition of 5 frames per wavelength interval. Figure 9 illustrates the spectral response of the RGB channels of image sensor equipped with the embedded two color filters and a single ND filter for spectral rectification, which shifted the peaks of each channel close to the 550 nm wavelength as the peak location of the luminosity function $V(\lambda)$ compared with Figure 7.

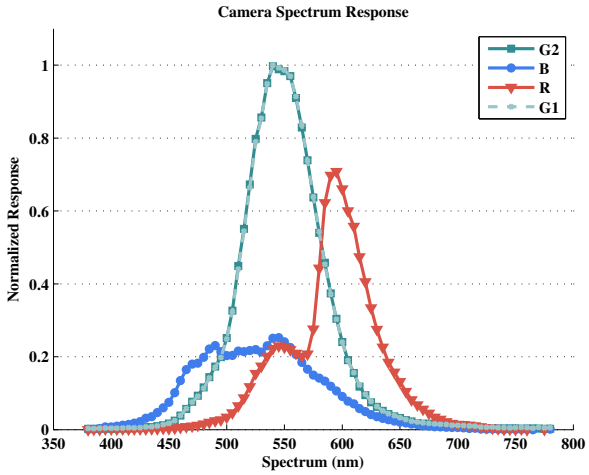


Fig. 9. Spectral response of the RGB channels after optical corrections

The luminosity function $V(\lambda)$ can be fitted through a linear transformation of the corrected spectral response of the imaging system equipped with filters. The coefficients of the RGB channels were determined by calculating the least-error in the $\ell_2$ norm space. With optimized coefficient of RGB channels, the spectral response of the imaging system is illustrated in Figure 10 and is close to the $V(\lambda)$ curve. According to the CIE publication No. 69 [56], the relative spectral correction error $f_1'$ was determined using Equations (1) and (2), where $S_l(\lambda)$ is the spectral distribution of illuminant (assumed CIE illuminant D65), $S(\lambda)$ is the relative spectral response of the detector, and $S_n(\lambda)$ is the normalized spectral response of the detector. The $f_1'$ error of the calibrated imaging system equipped with optical filters is equal to 8.89%, compared to 52.9% without optical corrections. According to the DIN 5032 standard [57], the maximum $f_1'$ error of a commercial luminance measurement device should be 9%, which achieved in this case.

$$f_1' = \frac{\int_{380}^{780} |\, S_n(\lambda) - V(\lambda) \,|\, d\lambda}{\int_{380}^{780} |\, V(\lambda) \,|\, d\lambda} \tag{1}$$

$$S_n(\lambda) = \frac{\int_{380}^{780} S_l(\lambda) V(\lambda)\, d\lambda}{\int_{380}^{780} S_l(\lambda) S(\lambda)\, d\lambda} S(\lambda) \tag{2}$$

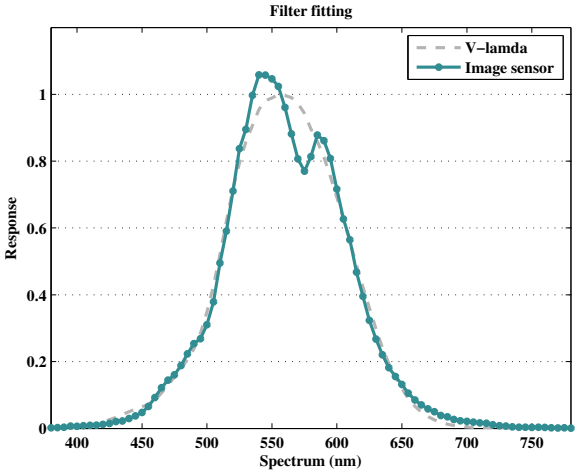


Fig. 10. Synthesised spectral response of the imaging system

### 3.2. Vignetting

Vignetting effect is essentially a phenomenon of imaging systems where the the intensity of light is attenuated towards off-axis zones; this is particularly noticeable at the edges of a frame with wide-angle lens. Multiple impact factors involved can be categorized into natural vignetting, optical vignetting, pixel vignetting and mechanical vignetting [58]. Natural vignetting is an intrinsic property of the lens that attenuates incident rays at off-axis parts, which obeys the $cos^4$ law of the off-axis angle $\alpha$ [58], as in Equation (3), where E is the illuminance at center and $E(\alpha)$ is that at off-axis pixels on the image plane. Optical vignetting is caused by the limited size of a lens and thus the clipping of light by the body of the lens, which can be potentially alleviated by introducing an aperture. Digital image sensors can also have pixel vignetting due to the occlusion by the walls of each photo-diode. In addition, the filters or the hood of a lens can contribute to mechanical vignetting.

$$E(\alpha) = E \cdot cos^4(\alpha) \tag{3}$$

For a fish-eye lens, the vignetting is inevitably an pronounced problem, which need to be corrected and compensated. The glass filters, as shown in Section 3.1, were placed behind the lens to reduce its mechanical vignetting. The existing vignetting was then measured and corrected using the experimental set-up illustrated in Figure 11. The integration sphere was employed to diffuse the light beam homogeneously in all directions at its exit port, which was used as the reference target to quantify the fall-off of intensity.

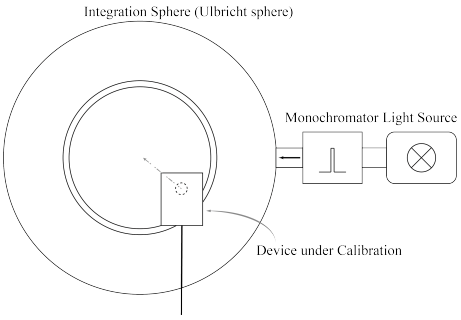


Fig. 11. Diagram of experimental set-up

To mitigate the temporal noise, 5 images were taken and averaged together. The lens was assumed to be axial symmetric and thus only a quarter of the image plane needed to be analysed, the remaining three quarters being deduced. The original signal turned out to be noisy with high density of spikes. In order to eliminate such noise, a 2-D Gaussian filter was applied through a convolution of the signal, as shown in Figure 12, where the signal surface was smoothed. Its normalized isoheight plane was illustrated by the color gradient, in which light intensity can be noticed being impaired from the origin (the center of image plane) to the boundary.

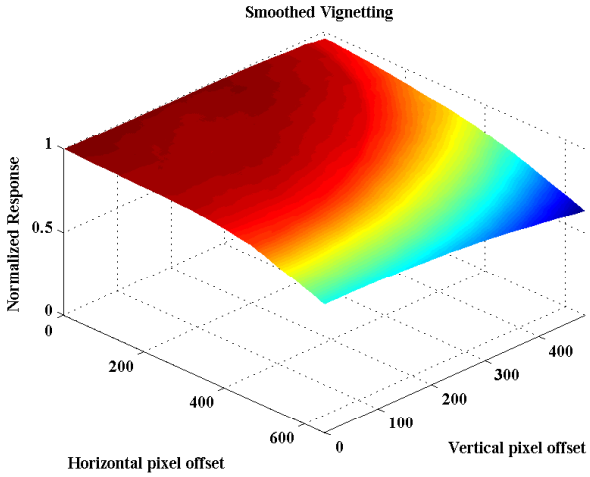


Fig. 12. Surface of response attenuation due to vignetting

Using the normalized surface of attenuation, the vignetting was approximated by a 4th-order polynomials of $cos(\alpha)$ to describe the combined effect of multiple factors, where $\alpha$ represents the off-axis angle, as given in Equation (4). The RGB channels were merged using the coefficients in Section 3.1 for calculating the value of normalized luminance V in Equation (4). Optimized with the least-error in the $\ell_2$ norm space, the function was fitted over the 2-D surface. The fitting results are partially illustrated in Figure 13 with deviation from the center in 1-D along the cross section of the horizontal axis on the image plane. The coefficients are listed in Table 1. The relative RMSE is equal to be 2.2%, and the $R^2$ coefficient of determination is equal to 0.961.

$$V = \sum_{i=0}^{4} a_i \cdot cos^i(\alpha) \tag{4}$$

*Table 1: Optimized coefficients*

| $a_0$ | $a_1$ | $a_2$ | $a_3$ | $a_4$ |
|---|---|---|---|---|
| 1.42 | -12.1 | 33.4 | -32.0 | 10.3 |

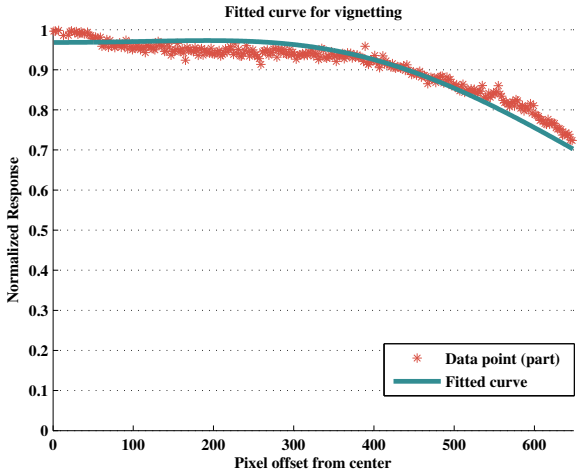


Fig. 13. Fitted curve for vignetting effect

### 3.3. Response curve

Linear response, in many ways, is a compelling system property, since it offers simplicity in both modelling and computing. Although the linear region of a photo-diode is commonly used to measure the number of captured photons, gamma correction is usually employed by camera manufacturers to compress the response of pixels in order to match the non-linear nature of the sensation of human eyes. An experiment was performed to evaluate the response curve and the linear region of the image sensor. The set-up is illustrated in Figure 14 where a class-B luminance meter (Minolta LS-110, with ±2% accuracy) substitutes the spectroradiometer to quantify the luminance of light as a reference. The shutter of the image sensor was set at 6 different speeds from 125 ms to 4 s so that both the saturated region and non-responsive region were covered respectively. The luminance at the exit port of the integration sphere was adjusted to range from 150 to 3900 cd/m$^2$.

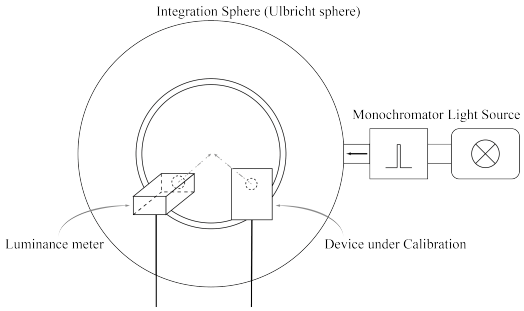


Fig. 14. Diagram of experimental set-up

The response curve of the RGB channels is illustrated in Figure 15. The response of each channel shows conspicuous linearity from above the noise floor upto a 3300 gray-scale value. Only the linear region of the response curve was used as a valid sensing range for luminance detection. Together with the weightings of RGB channels obtained in Section 3.1, the luminance L measured by a group of 4 neighbouring pixels (R,G1,G2,B) can be fitted by Equation (5) according to the integration time $\triangle t$, where $C_g$ is the coefficient to be determined and R G B are the gray-scale values of corresponding pixels and G is the mean of $G_1$ and $G_2$. Using the least-square norm as the objective function, the optimized coefficient $C_g$ was computed with data points pertaining only to the linear response region. The corresponding fitted response curve with data points is presented in Figure 16 a). The relative error compared to the reference luminance given by the luminance meter is illustrated in Figure 16 b); it is bounded by 2% and shows a mean relative error of 0.81%.

$$L = C_g \cdot \frac{w_1 R + w_2 G + w_3 B}{\triangle t} \tag{5}$$

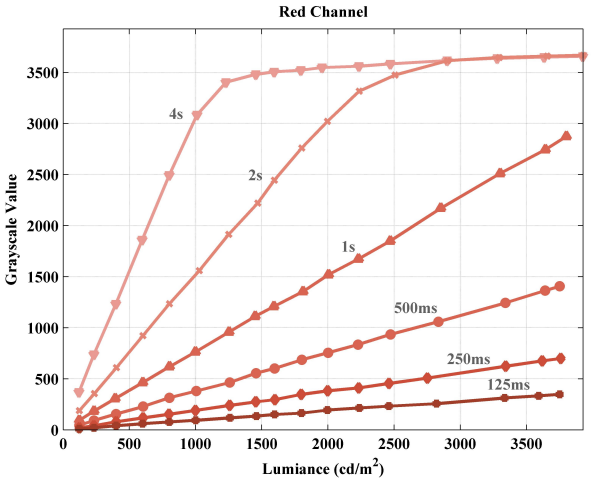


(a) Red channel

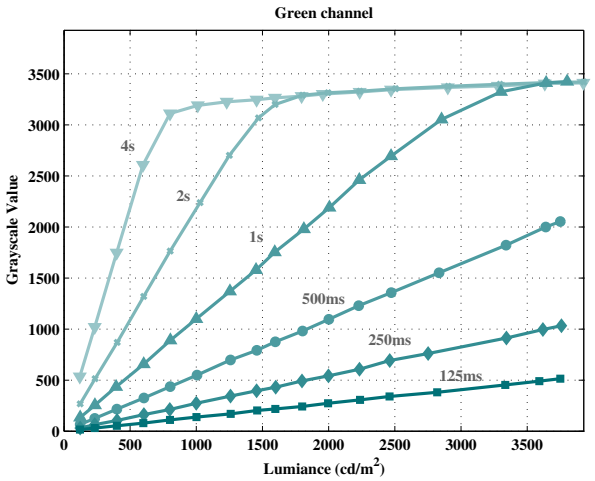


(b) Green channel

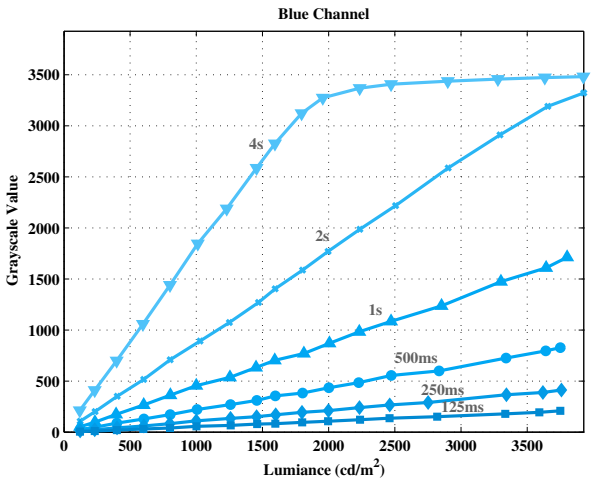


(c) Blue channel

Fig. 15. Response of RGB channel versus luminance at 6 shutter speed

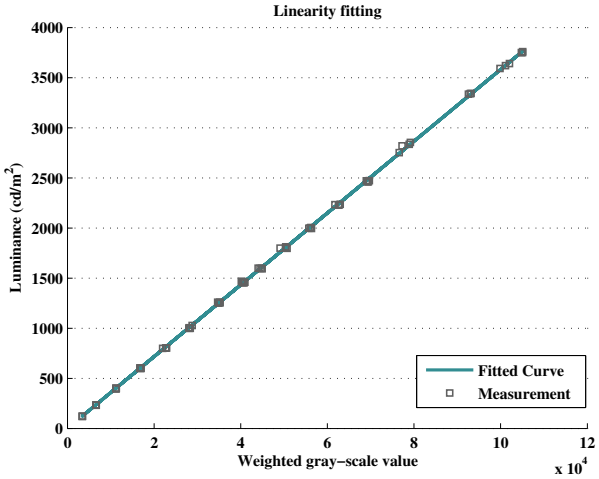


(a) Fitted curve

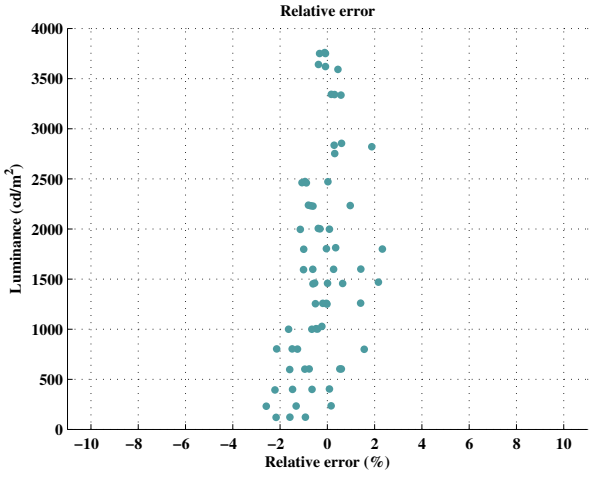


(b) Relative error distribution

Fig. 16. Luminance monitoring by the calibrated imaging system and its error distribution

Owning to the imperfection of the lens, an imaging system with a wide-angle lens also suffers from linear and non-linear distortions. A field-test experiment with a standard chessboard was conducted first to determine the distortion coefficient and correct it during computation. Above all, the imaging system was corrected with optical glass filters for its spectral response and rectified digitally for its vignetting, response curve and geometric distortion. The device is able to cover a luminance detection range of $3.78 \times 10^9 \sim 1.2 \times 10^2$ cd/m$^2$ (150 dB), the maximal mapping resolution reaching 1.2 million pixel groups, each pixel group being able to sense one single subdivided sky patch.

## 4. Empirical validation

The usual daylight simulation approach is based on standard sky models, their oversimplification contributing to a noticeable mismatch compared to a real sky and therefore commonly to pronounced simulation errors [59], when the time scale is at the level of minutes or even seconds. By substantially expanding the volume of input data and thus increasing the resolution of the sky luminance scanning, the HDR imaging based sky luminance monitoring technique can reduce the discrepancy with real skies, which features complex patterns of clouds, high contrast sky regions as well as the direct sun orb. The ground is another factor contributing to simulation errors. A common practice is to model it as a lower hemisphere fraction with a 20% typical constant reflectance. In fact, the ground is complex in reality. Its reflectance is manifold and variable; it can reach as low as 7-9% for clean asphalt or slate and as high as 60-80% for snow. In addition, it is problematic to model the surrounding buildings or vegetation as a flat surface or an homogeneous hemisphere. The HDR luminance monitoring method can potentially reduce the discrepancy by real-field measurement in high resolution, which at the same time saves the efforts in modelling the landscape. After deliberate calibrations and parameter optimization, the embedded photometric device is able to map both the sky vault and ground in a subdivision with 1.2 million luminance patches, and its wide luminance detection range is able to cover the luminance at two extremes of both the direct solar orb and surrounding shadowing objects. This section evaluates its performance regarding the accuracy in physically based rendering, horizontal illuminance computing, and solar position tracking and intensity monitoring.

### *4.1. Rendering*

Merging every 4 neighbouring pixels into a group, the image sensor with 5 million pixels was divided into 1.23 million groups, each detecting the luminance of a patch of the sky vault or the ground in an unique direction from the lens. Multiple exposures (0.5$s$ in total) of the image sensor were controlled and image acquisition was pre-processed by the FPGA fabric part of the processor. Then the HPS part of the processor synthesised multiple frames into luminance values and mapped each pixel onto a single sky or ground patch, based on the parameters acquired in Section 3. The resolution of luminance mapping is variable and can be downgraded by sub-sampling with the application of low-pass digital filters for anti-aliasing effects. In the context of this paper, the maximal resolution was retained for the evaluation of accuracy performance. Since the focal length (2.5 mm) of the lens is infinitesimal compared to the object distance (to the principal plane) in the camera coordinates, including the sky, the sun disk, clouds, and landscape on the ground, objects can approximately be regarded as a single entity and the lens can focus on the infinity. It takes the processor 1.3 seconds to accomplish the whole course of HDR imaging acquisition, data processing, and luminance mapping.

For image rendering of a scene, the RADIANCE program, a physically-based lighting simulation program package largely developed by Greg Ward [60], was employed in this paper with the backward ray-tracing algorithms computing the daylighting of buildings. The two sub-programs, rtrace and rpict, were employed and run on the HPS part of the processor to render the scene.

A typical office with an unilateral façade was selected as the study target. The calibrated embedded device was positioned in front of the façades with its lens axis in the orthogonal plane of the façades. The FOV of the lens was aimed at the sky vault facing the façade. The absolute geographical coordinates of the test room are not necessary for the lighting computing, since the daylighting in the space was exclusively contributed by the light through the unilateral façades, and a relative coordinate was established for the imaging system with the sky vault and ground.

A 3-D model of the selected office space was created for the device. After the luminance map of the hemisphere seen by the camera, comprising half of the sky vault and half of the ground, was monitored, it was compiled with the scene model into an octree file for the RADIANCE program in the device. The embedded device was able to perform the rendering of the scene in 79.2 seconds with $1.41 \times 10^6$ tracing rays for a coarse image, with splotchy patterns in the shadowed zones. In fact, the computing time is largely contingent on the resolution of the luminance map. If the sky patches are sub-sampled into 145 patches according to the Tregenza or Klems subdivision [61], the time in rendering the same scene can be reduced to 1/3 of that in full resolution (20-30 s). With high quality parameters, maximal luminance map resolution, and long time rendering, the scene of the office was rendered with a smooth shadow on the wall as illustrated in Figure 17 b) for a partly cloudy sky. For comparison, the direct normal and diffuse horizontal irradiance was simultaneously measured on the rooftop of the office building, and a common practice employing the Perez all-weather sky model [39] using the monitored irradiance as inputs is illustrated in Figure 17 a) rendering the scene of the same office room. The merits of the HDR imaging based sky monitoring approach can be illustrated by the neat contour of the sky patterns and landscape from a viewing perspective towards the façades, including the surrounding buildings and vegetation which is extremely difficult to model correctly. In addition, the HDR imaging approach is closer to the reality than that employing the Perez sky model as in common practice according to the mismatch in the shadows on the desks and floor in Figure 17.

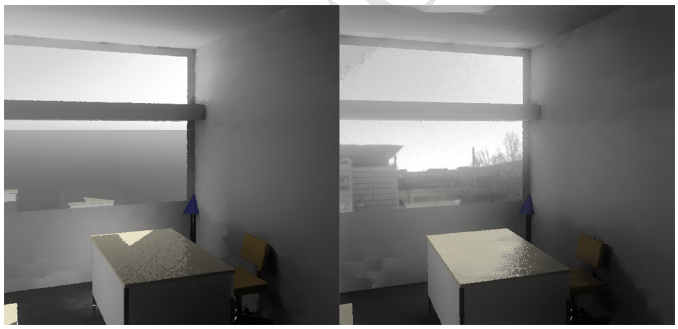

Fig. 17. Rendering of a office by a) Perez model b) HDR imaging based sky model

### 4.2. Horizontal Illuminance

While Section 4.1 qualitatively assessed the accuracy of the embedded device in daylighting image rendering, this section investigates the computation of intra-scene horizontal work-plane illuminance distribution, compared with the monitoring from an array of real lux-meters as a reference. In this section, the onboard RADIANCE program was used again for computing the illuminance distribution based on ray-tracing and Monte-Carlo integration techniques. In order to outline its performance, the embedded photometric device based on the HDR sky monitoring approach was compared with a common practice employing the Perez all-weather sky model based on weather data.

#### 4.2.1. Experimental set-up

A retrofitted lighting test module (interior size: $6.4 \times 2.9 \times 2.6\ m^3$) was selected as the experiment site, mimicking a typical office room with 3 pairs of desk and chair. The module was equipped with an unilateral façade (6 elements) facing towards south, showing a 0.62 window to wall ratio in total, as presented in Figure 18 a). To improve simulation accuracy, both the dimensions and the reflectance of each surface composing the module were modelled in accordance to reality. In this experimental set-up, the geometric dimensions and relative position of each furniture in the module were measured by using a precise range finder (Leica DISTO), establishing relative coordinates of all the objects. The chromatic coordinates and reflectance factors of each surface material was measured by using a chromameter (MINOLTA CR-220) in the xyY color space with a CIE D65 light source, including the ceiling, the wall, the floor, the window frame, and each furniture surface. As RADIANCE adopted the RGB color space, the measured xyY chromatic coordinates were converted into the RGB color space based on pre-defined primaries in RADIANCE by matrix multiplication. The specularity, characterizing the ratio of the direct component in reflection, was measured by using a gloss meter (MINOLTA GM-060). It characterized the proportion of specular component at the incident angle of 60° and was supposed to approximate the specularity, despite of its minor dependence on the incident angle. Furthermore, the roughness of each material was assigned a $0 - 0.2$ value according to the particle size of the surface. The virtual model of test module is illustrated in Figure 18 b).

(a) Real scene (b) Modelled scene

Fig. 18. The daylighting test module with unilateral façades

For the work-plane horizontal illuminance monitoring, five lux-meter sensors (MINOLTA T-10A, with ±2% accuracy) were

positioned in the test module at the workplane height of 0.8 m, with their sensible surface aligned upward in the horizontal plane. The sensors were arranged in a line and fixed at the distance of 1 m, 2 m, 3 m, 3.9 m and 4.7 m from the façade, as shown in Figure 19. Each lux-meter was connected in parallel to a data logger ensuring that the measurement from each sensor can be acquired simultaneously. Accordingly, for the daylighting simulation, 5 virtual sensors were placed at identical positions in the modelled scene as in the real module. Since the virtual sensors were point receptors in RADIANCE, 9 sampling points covering a $2 \times 2\ cm^2$ square were defined and averaged to reproduce the sensing area of each lux-meter and to reduce the spatial noise for the computing.

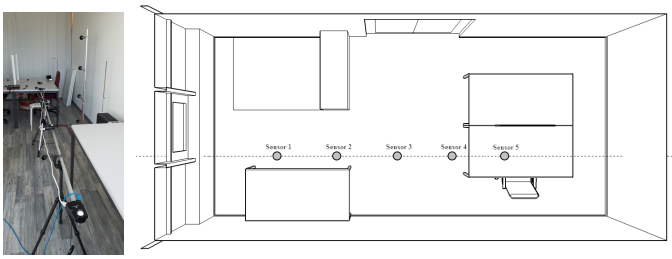


(a) Lux-meter (b) Virtual illuminance sensors defined in RADIANCE

Fig. 19. Sensor position for monitoring horizontal illuminance

During the experiments, three major equipments were installed close to the daylighting test module: the HDR embedded photometric device (under test), a pyranometer (Delta-T BF3) monitoring the direct normal and diffuse horizontal irradiance (for comparison with the Perez sky model) and a lux-meter array (for the acquisition of reference illuminance values), as illustrated in Figure 20.

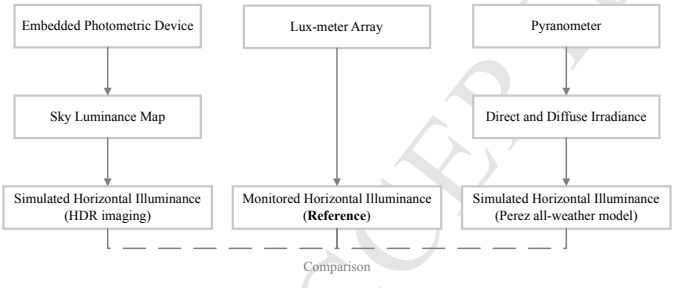


Fig. 20. Employed equipments and their feature in experiments

The embedded device was anchored in front of the test module with its lens axis aligned in the plane orthogonal to the façade, as illustrated in Figure 21. The device was adjusted with 2/3 of its FOV covering the sky vault and 1/3 of that covering the ground fraction, as the sky is responsible for the main daylighting contribution through the façade. The process of HDR sky and landscape monitoring, luminance mapping, and computation of horizontal illuminance distribution were executed on-board independently. The pyranometer was positioned on the rooftop without shadowing. Its monitoring of the direct normal and diffuse horizontal irradiance was used as input for the Perez all-weather sky model during the simulation of the workplane illuminance distribution. The three apparatus were synchronized during the data monitoring, in order to achieve simultaneous illuminance simulations and measurements. To reach a high accuracy, identical sets of simulation parameters in RADIANCE were employed based on the backward ray-tracing and Monte-Carlo integration techniques for both the HDR imaging approach and Perez sky model respectively, with '-ab 5 -ad 1024' for ambient calculation. As a trade-off between computation accuracy and time consumption, the synchronization was made using 15 min sampling time intervals for the three apparatus.

Fig. 21. The embedded photometric device positioned in front of the unilateral façade

To study the accuracy of the simulated workplane illuminance using the embedded photometric device, partly cloudy days with predominant overcast and clear sky, when most of the time during the day was dominated by overcast or clear sky, and the rest of time it was partly cloudy, were considered as the two critical conditions to investigate daylighting without artificial lighting inside. The experiments were conducted from 9 a.m. to 6 p.m. in the test module from May $08^{th}$ to $09^{th}$, 2017 in Lausanne, Switzerland; the workplane horizontal illuminance was both simulated by the device and measured by using the lux-meter array.

### *4.2.2. Predominant overcast sky*

The workplane horizontal illuminance computed by the lighting software with the use of the embedded photometric device based on HDR sky luminance monitoring is illustrated in Figure 22 a) by the green solid lines for a predominant overcast sky. The five curves stacked sequentially from top to bottom respectively for the illuminance values simulated for points at a 1 m distance to a 4.7 m distance from the façade. The corresponding monitored horizontal illuminance are denoted by the grey dotted lines and used as reference values to assess the simulation error. Analogously, the workplane horizontal illuminance simulated by the virtual sensors using the Perez all-weather model is represented by green lines in Figure 22 b). Although the monitored illuminance of each lux-meter fluctuated throughout the day, the HDR sky monitoring approach outperformed the Perez sky model by leading to simulated workplane illuminances which were closer to the monitored value,

used as reference (grey dotted line) as shown in Figure 22 a) and b). Using the illuminance monitored by the lux-meters as reference, the relative error of the two methods was determined, and Figure 23 illustrates the results for the 5 sensors denotes by gradient shaded bars and grouped along the time line for Sensor 1 at distance of 1 m and Sensor 5 at distance of 4.7 m from the façade respectively. The relative error bars are showing the advantage of employing the HDR sky monitoring approach compared to the simple sky model. The average error of the five workplane illuminance computed using the HDR sky luminance monitoring approach in case of a predominant overcast sky are equal to 6.4%, 7.5%, 4.1%, 5.0%, and 7.0% respectively; those obtained by the Perez sky model are reaching respectively 32%, 22%, 29%, 23% and 23%. The overall 3-4 times higher error rate of the Perez sky model can be explained by the fact that it neglects high contrast patches of the sky vault and the ground fraction, where the complex clouds patterns and non-smooth nature of the landscape are commonly major factors for errors.

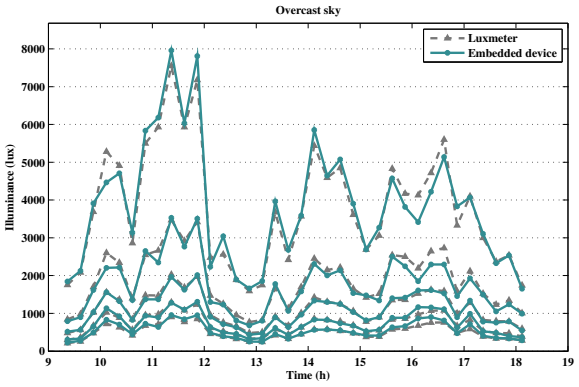


(a) HDR imaging approach

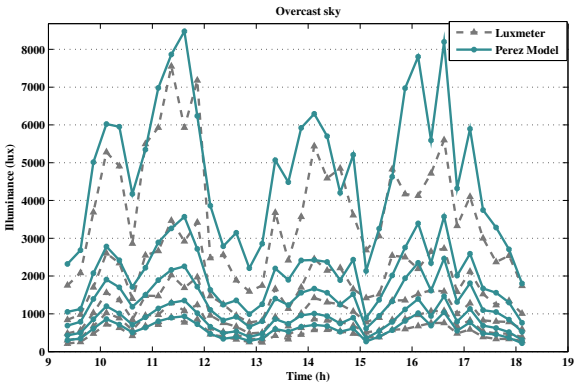


(b) Perez all-weather sky model

Fig. 22. Workplane horizontal illuminance assessed by two daylighting simulation methods compared with lux-meters values for an overcast sky [62]

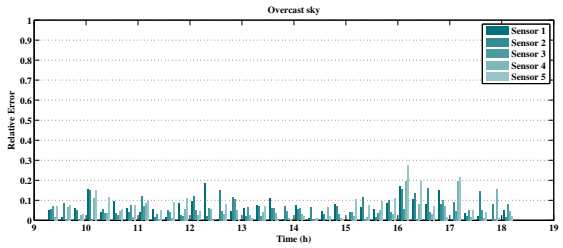


(a) HDR imaging approach

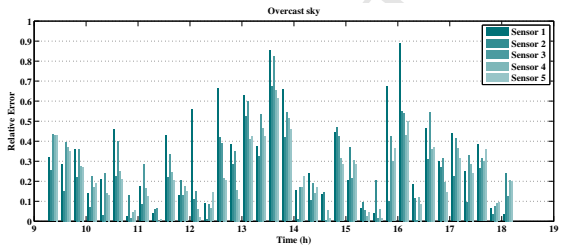


(b) Perez all-weather sky model

Fig. 23. Relative error of the 5 computed workplane illuminances compared with lux-meter values for an overcast sky [62]

### *4.2.3. Predominant clear sky*

For a predominant clear sky, the horizontal illuminance on the workplane based on the HDR sky luminance monitoring approach issued from the embedded photometric device is illustrated in Figure 24 a), the stacked lines representing the 5 computed values (green) as well as reference values by lux-meters (grey) at identical positions respectively. Similar to Section 4.2.2, the simulated workplane illuminance based on the Perez sky model are shown in Figure 24 b) together with the monitored illuminance values (grey). According to their mismatch with the reference values, the HDR imaging based sky luminance monitoring approach shows higher concordance with the monitored illuminance values than the common practice employing the Perez sky model, thanks to the high resolution sampling inputs. The relative error regarding the reference was also calculated and is illustrated in Figure 25 a) and b) for the two approaches respectively. The Perez all-weather sky model approach shows overall a larger error rate than the HDR sky luminance monitoring approach in the transient daylighting simulation, which is likely due to the oversimplification of sky models which are levelling the high contrast patches of the sky vault and the ground fractions. It can also be noted from the figure, on the time line 13:00 - 14:00, when the sun was occluded by thin clouds, that the relative error of the Perez model exceeded 100%, i.e. the sky model shows a pronounced discrepancy in regards to the real sky; on the opposite, the HDR sky monitoring approach must be given merits for its accuracy; however, for the sake of clarity and comparison of the error bars, Figure 25 was not scaled down to include the highest peaks. The average over-all relative error of the 5 computed illuminances throughout a day with a pre-dominant clear sky is respectively equal to 25%, 22%, 9.7%, 8.9%, and 11% for the HDR imaging based sky monitoring approach and 37%, 32%, 36%, 31%, and 28% for using the Perez all-weather sky model. Although the

former approach shows lower relative errors than the latter, the first two simulated illuminances, at 1 m and 2 m distance from the façade, for the HDR imaging based approach, were prone to noticeable errors compared with the other three locations deep into the test module, which can also be noted from the time line 9:00-11:00 in Figure 25 a), when the sky was entirely clear without any thin clouds occluding the sun. This can possibly be attributed to the insufficient sampling of the sun disk, since for a clear sky, the solar disk is one of the major sources of daylighting. The sky background together with the sun was defined as the 'glow' material in RADIANCE program, which sampled randomly the sky vault. With a low probability for sampling rays to reach the solar disk due to its relatively small dimension, there is a high probability of underestimating the overall sky luminance as well as the corresponding daylighting contribution in the test module.

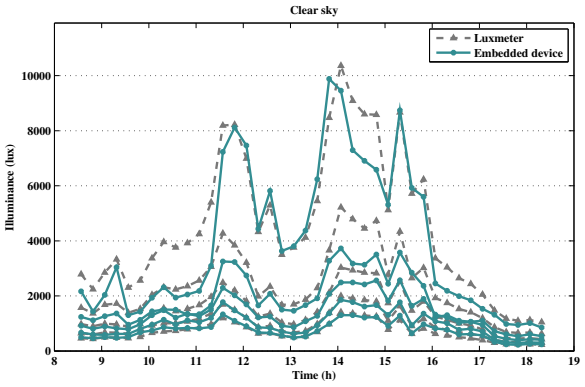


(a) HDR imaging approach

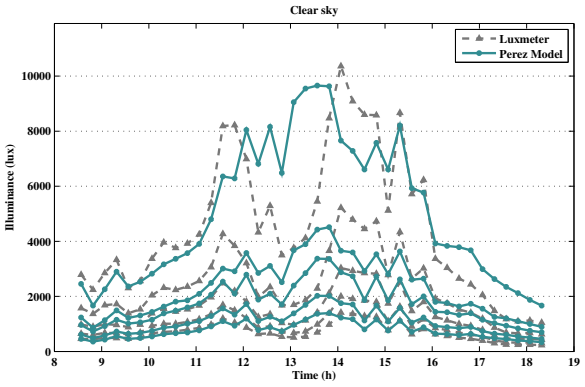


(b) Perez all-weather sky model

Fig. 24. Workplane horizontal illuminance assessed by two daylighting simulation methods with lux-meters values for a clear sky [62]

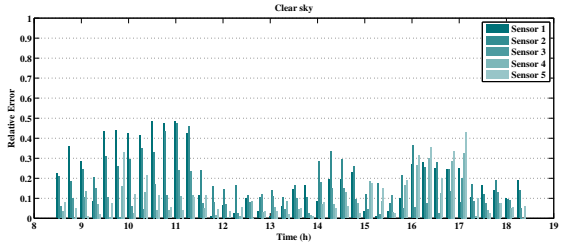


(a) HDR imaging approach

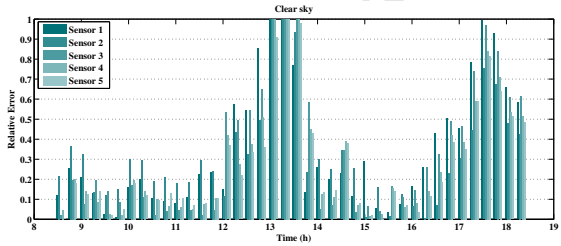


(b) Perez all-weather sky model

Fig. 25. Relative error of the 5 computed workplane illuminances compared with lux-meter values a clear sky [62]

#### 4.2.4. *Improvement of sampling*

The issue of insufficient sampling of the high contrast sun disk for a clear sky can be addressed by the extraction of the solar patch and by using concentrated sampling. As the maximal luminance of the sun orb observed at sea-level in a clean atmosphere is around $1.6 \times 10^9$ $cd/m^2$ [63], the extraction of the solar disk was based on a threshold of solar luminance of $5 \times 10^8$ $cd/m^2$, as well as a subtending angle on the monitored luminance map from the embedded device equal to 0.53° in the FOV. The extracted sun disk is defined as a separated component in RADIANCE as a 'light' instead of a 'glow' material for the concentrated sampling on the sun. With this improvement, the experiment with the embedded device was repeated on another day with a predominant clear sky from 10:00 - 18:00, the sky condition being clearer (less thin cloud presence) than that in Section 4.2.3. The workplane horizontal illuminance of the 5 virtual sensors are illustrated in Figure 26 and compared to the reference values monitored by lux-meters. The two front locations, at 1 m and 2 m distance from the façade, show better concordance and a lower discrepancy with the reference illuminance values than those shown in Figure 24 a). The relative error for the two virtual sensors, as presented Figure 27, are significant reduced, compared to Figure 25 a). The average error throughout a day with a clear sky is improved respectively to 7.5%, 6.1%, 8.7%, 5.3%, and 8.2% for the HDR imaging based sky monitoring approach in comparison to the results presented in Section 4.2.3.

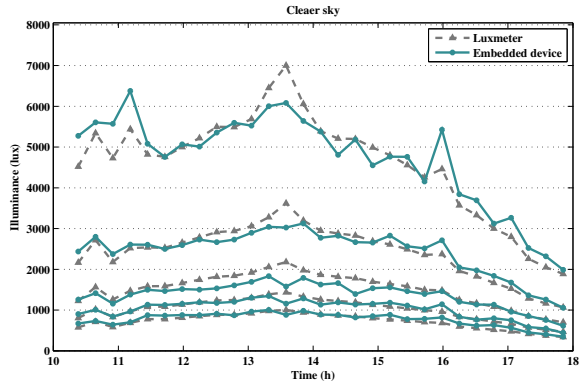


(a) HDR imaging approach with improved sampling

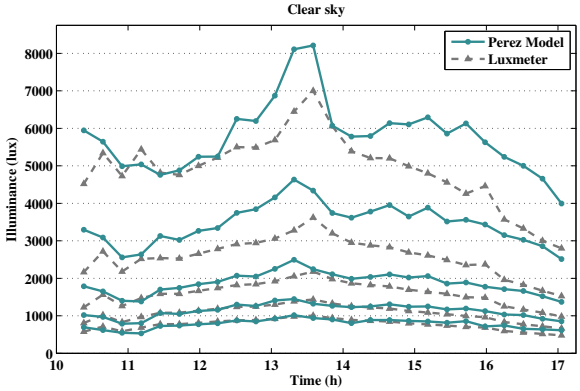


(b) Perez all-weather model

Fig. 26. Workplane horizontal illuminance assessed by two daylighting simulation methods with lux-meters values for a clear sky

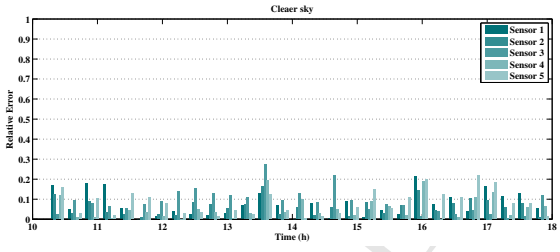


(a) HDR imaging approach with improved sampling

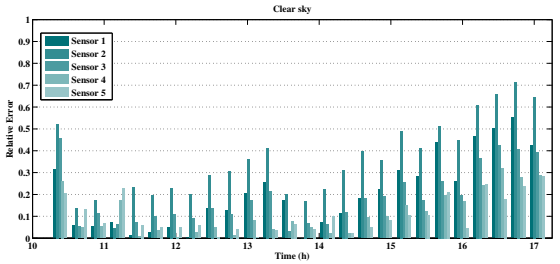


(b) Perez all-weather sky model

Fig. 27. Relative error of the 5 computed workplane illuminances compared with lux-meter values for a clear sky

### *4.3. Solar tracking*

The solar orb providing a substantial contribution to the daylighting in buildings during clear sky conditions, an accurate mapping of the solar disk from the image plane to the world coordinates would have a noticeable influence on the overall accuracy of daylight simulation based on the embedded photometric device. This section presents the evaluation of the monitoring accuracy of the sun orb by the embedded device, with regard to solar luminance and position.

The device was positioned with the lens axis aligned towards the south, as shown in Figure 21. The solar position was determined according to centroid of a group of pixels on the luminance map with values larger than the threshold defined in Section 4.2.4; their size corresponded to 0.53° angle FOV. The luminance of the solar patch was assessed by averaging 35 pixel groups identified according to its luminance, and subtending 0.53° in the FOV. According to its position on the image plane, the sun location was determined by applying the intrinsic and extrinsic matrix of the imaging system [64]. As reference, the solar luminance was also measured indirectly by using a pyranometer that recorded the global and diffuse horizontal illuminance, and it was converted to solar luminance according to the solar position. The zenith angle (solar altitude) $a_t$ and azimuth angle $a_s$ of the sun can be calculated by Equation (6).

$$\begin{aligned} a_t &= arcsin(sin(l)sin(\delta) - cos(l)cos(\delta)cos(\pi t/12)) \\ a_s &= arctan[\frac{-cos(\delta)sin(\pi t/12)}{-(cos(l)sin(\delta) + sin(l)cos(\delta)cos(\pi t/12))}] \end{aligned} \quad (6)$$

where t is the solar time in decimal hours, l is the site latitude in radians and $\delta$ is the solar declination in radians, defined by $\delta = 0.4093 sin(2\pi(J - 81)/368)$, where J is the Julian date [65]. The calculation of the sun position is based on the results obtained by National Oceanic and Atmosphere Administration (NOAA).

During one day with predominant clear sky on Jun. $23^{th}$, 2017, the embedded photometric device tracked the sun luminance and position every 15 min from 10:00 to 18:00. The monitored solar luminance is illustrated in Figure 28 a) by a green solid line, and compared to the reference measurement obtained by a pyranometer (grey dotted line). Accordingly, the sun zenith and azimuth angle monitored by the embedded device are illustrated in Figure 28 b) and c) respectively (green solid lines), together with the reference data (e.g. NOAA and pyranometer, in grey dotted lines). The average relative error (RMSE) throughout a day for the luminance of the solar disk monitored by the embedded device is equal to 9.6% and those of the elevation angle and azimuth angle are equal to 2.4% and 1.3% respectively, demonstrating its reliability and accuracy in solar tracking.

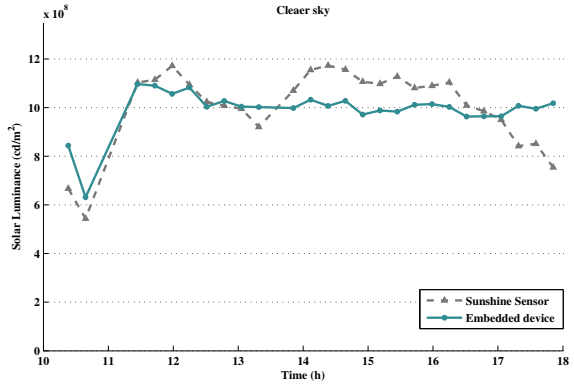


(a) Solar Luminance

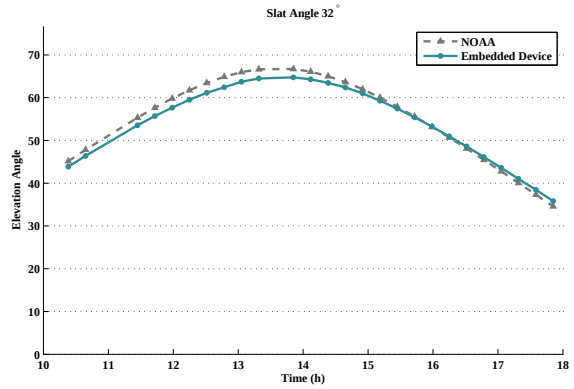


(b) Elevation angle of the sun

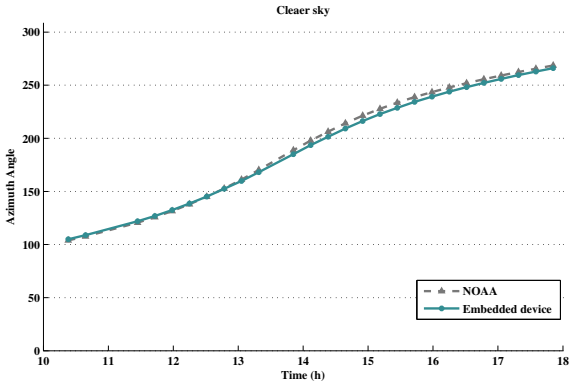


(c) Azimuth angle of the sun

Fig. 28. Solar luminance and position monitored by embedded photometric device

## 5. Conclusion

The accuracy of daylighting simulation can be strongly influenced by the mismatch between the luminance distribution of standard sky models used in simulation and that of real skies. By monitoring the luminance of the sky vault and the ground fraction with a high resolution mapping, this mismatch can be substantially reduced especially when the time scale for simulation reaches minutes or even seconds, in this way overcoming the limitation of standard sky models, most of which are based on weather data and average conditions obtained over multi-annual periods among various geographical locations. This paper presents a compact embedded photometric device comprising a FPGA processor and an image sensor used for real-time on-board daylighting simulations following an HDR sky luminance monitoring process.

A calibration procedure of the imaging system was designed and validated with experimental data issued from the luminance monitoring of the sky vault. The calibration procedure includes the spectral response, vignetting effect, response and geometric distortion of the imaging system. Its spectral response was rectified by a short-pass and a long-pass filter, improving the relative spectral correction error $f_1'$ to 8.89%. The vignetting effect and geometric distortions were corrected and compensated by the processor. The dynamic range of the imaging system reaches 150 dB, covering a luminance monitoring range between $3.78 \times 10^9 \sim 1.2 \times 10^2$ cd/m$^2$: the upper bound is high enough to monitor the extreme luminance of the sun orb and the lower bound is low enough to perceive a relatively dim landscape during daytime. This high resolution imaging system is able to map the sky vault and the ground fraction in $1.2 \times 10^6$ patches, which potentially alleviate the difficulty in modelling landscape, including buildings and vegetation.

The performance of the device was demonstrated using 'in situ' experiments in daylighting test modules for image rendering, horizontal illuminance simulation and solar tracking. Firstly, the device was able to accomplish an HDR sky monitoring, luminance mapping and on-board image rendering in 79.2 s tracing $1.41 \times 10^6$ rays, using the on-board RADIANCE programs. The rendering of façades with outdoor views of the landscape showed a better concordance with reality compared to a common practice simulation employing the Perez all-weather model. Secondly, the accuracy achieved with the embedded photometric device used in daylighting simulation on the workplane horizontal illuminance was assessed comparing to a common practice employing the Perez all-weather model, using measurements by a lux-meter array as reference. For both predominant overcast and clear sky conditions, the embedded photometric device based on HDR sky monitoring was able to reduce the error of transient workplane illuminance calculation to $\frac{1}{7} \sim \frac{1}{3}$ of that of the common practice using standard sky models. The simulation accuracy was demonstrated experimentally to be improved thanks to the extraction of the solar direct component and application of concentrated sampling method for clear sky conditions. Finally, the device showed a quality in solar tracking, with relative average error 9.6% for solar luminance monitoring and below 3% in the sun position tracking.

Above all, the embedded photometric device demonstrated its merits in real-time daylighting simulations, in the response time, simulation quality, and adaptability. In the context of building automation, the device can potentially be used for the control of shading, lighting or electro-chromic glazing to regulate daylight penetration and passive solar heat gain both for centralized and decentralized systems. Moreover, its capability in solar luminance monitoring and position tracking make

it suitable for the solar photovoltaic (PV) power generation or control of the profile angle of the modules. In addition, the device accuracy in daylighting simulation can also be used for the analysis of lighting solutions in retrofitting process. If the resolution of the luminance map is downgraded to 145 Tregenza or Klems patchs, the 5-phase matrix algebraic approach [66] would be employed to save computational resources, using pre-computed view matrix and inter-reflection matrices, the FPGA fabrics can be exploited to parallelize the computation massively. Investigation on its reliability and on its ability to accelerate the computing by employing the FPGA fabric part will be the subject of future work.

## 6. Acknowledgement

This research project is financially supported by the Swiss Innovation Agency Innosuisse and is part of the Swiss Competence Center for Energy Research (SCCER FEEB&D).

## References

[1] E. H. Borgstein, R. Lamberts, Developing energy consumption benchmarks for buildings: Bank branches in brazil, Energy and Buildings 82 (Supplement C) (2014) 82 – 91.

[2] M. Levine, D. Fridley, H. Lu, C. Fino-Chen, Key china energy statistics 2011, Tech. rep., Lawrence Berkeley National Lab.(LBNL), Berkeley, CA (United States) (2012).

[3] A. Reinders, J. C. Diehl, H. Brezet (Eds.), The Power of Design: Product Innovation in Sustainable Energy Technologies, John Wiley Sons, West Sussex, UK, 2012.

[4] L. Halonen, E. Tetri, P. Bhusal (Eds.), Guidebook on Energy Efficient Electric Lighting for Buildings, Aalto University School of Science and Technology, Espoo, Finland, 2010.

[5] An assessment of energy technologies and research opportunities, Quadrennial technology review, Department of Energy, USA (Sept 2015).

[6] M. A. ul Haq, M. Y. Hassan, H. Abdullah, H. A. Rahman, M. P. Abdullah, F. Hussin, D. M. Said, A review on lighting control technologies in commercial buildings, their performance and affecting factors, Renewable and Sustainable Energy Reviews 33 (Supplement C) (2014) 268 – 279.

[7] J. C. Lam, D. H. Li, S. Cheung, An analysis of electricity end-use in air-conditioned office buildings in hong kong, Building and Environment 38 (3) (2003) 493 – 498.

[8] G. Lowry, Energy saving claims for lighting controls in commercial buildings, Energy and Buildings 133 (Supplement C) (2016) 489 – 497.

[9] A. Williams, B. Atkinson, K. Garbesi, F. Rubinstein, E. Page, A meta-analysis of energy savings from lighting controls in commercial buildings, Tech. rep., Ernest Orlando Lawrence Berkeley National Laboratory, Berkeley, CA (US) (2011).

[10] S. N. Kamaruzzaman, R. Edwards, E. M. A. Zawawi, A. I. Che-Ani, Achieving energy and cost savings through simple daylighting control in tropical historic buildings, Energy and Buildings 90 (Supplement C) (2015) 85 – 93.

[11] D. Salem, E. Elwakil, Daylighting-based assessment of occupant performance in educational buildings, Journal of Professional Issues in Engineering Education and Practice 143 (1) (2017) 04016014.

[12] A. Tsangrassoulis, A. Kontadakis, L. Doulos, Assessing lighting energy saving potential from daylight harvesting in office buildings based on code compliance & simulation techniques: A comparison, Procedia Environmental Sciences 38 (2017) 420 – 427, sustainable synergies from Buildings to the Urban Scale.

[13] Y. F. Lian, Lighting energy-saving design for industrial factory building, in: Green Power, Materials and Manufacturing Technology and Applications III, Vol. 484 of Applied Mechanics and Materials, Trans Tech Publications, 2014, pp. 737–741.

[14] S. Chun, C.-S. Lee, J.-S. Jang, Real-time smart lighting control using human motion tracking from depth camera, Journal of Real-Time Image Processing 10 (4) (2015) 805–820.

[15] L. Song, G. Y. Yao, Design of library lighting energy saving system based on internet of things, in: Frontiers of Manufacturing and Design Science IV, Vol. 496 of Applied Mechanics and Materials, Trans Tech Publications, 2014, pp. 1690–1693.

[16] J. Liu, W. Zhang, X. Chu, Y. Liu, Fuzzy logic controller for energy savings in a smart led lighting system considering lighting comfort and daylight, Energy and Buildings 127 (Supplement C) (2016) 95 – 104.

[17] M. Wei, S. Chen, Impact of spectral power distribution of daylight simulators on whiteness specification for surface colors, Color Research & Application n/a–n/a.

[18] S. M. Pauley, Lighting for the human circadian clock: recent research indicates that lighting has become a public health issue, Medical Hypotheses 63 (4) (2004) 588 – 596.

[19] C. Cajochen, Alerting effects of light, Sleep Medicine Reviews 11 (6) (2007) 453 – 464.

[20] M. Andersen, S. J. Gochenour, S. W. Lockley, Modelling non-visual effects of daylighting in a residential environment, Building and Environment 70 (Supplement C) (2013) 138 – 149.

[21] M. L. Amundadottir, S. Rockcastle, M. S. Khanie, M. Andersen, A human-centric approach to assess daylight in buildings for non-visual health potential, visual interest and gaze behavior, Building and Environment 113 (Supplement C) (2017) 5 – 21, advances in daylighting and visual comfort research.

[22] R. G. Stevens, D. E. Blask, G. C. Brainard, J. Hansen, S. W. Lockley, I. Provencio, M. S. Rea, L. Reinlib, Meeting report: the role of environmental lighting and circadian disruption in cancer and other diseases, Environmental health perspectives 115 (9) (2007) 1357.

[23] G. Costa, The impact of shift and night work on health, Applied Ergonomics 27 (1) (1996) 9 – 16, shiftwork.

[24] S. S. Intille, Designing a home of the future, IEEE pervasive computing 1 (2) (2002) 76–82.

[25] M. Hillman, J. Parker, More daylight, less electricity, Energy Policy 16 (5) (1988) 514 – 515.

[26] J. Strmann-Andersen, P. Sattrup, The urban canyon and building energy use: Urban density versus daylight and passive solar gains, Energy and Buildings 43 (8) (2011) 2011 – 2020.

[27] A. Mavrogianni, M. Davies, J. Taylor, Z. Chalabi, P. Biddulph, E. Oikonomou, P. Das, B. Jones, The impact of occupancy patterns, occupant-controlled ventilation and shading on indoor overheating risk in domestic environments, Building and Environment 78 (Supplement C) (2014) 183 – 198.

[28] L. Sanati, M. Utzinger, The effect of window shading design on occupant use of blinds and electric lighting, Building and Environment 64 (Supplement C) (2013) 67 – 76.

[29] M.-C. Dubois, ke Blomsterberg, Energy saving potential and strategies for electric lighting in future north european, low energy office buildings: A literature review, Energy and Buildings 43 (10) (2011) 2572 – 2582.

[30] Lighting energy savings potential of split-pane electrochromic windows controlled for daylighting with visual comfort, Energy and Buildings 61 (2013) 8 – 20.

[31] K. Konis, Evaluating daylighting effectiveness and occupant visual comfort in a side-lit open-plan office building in san francisco, california, Building and Environment 59 (2013) 662 – 677.

[32] J. McArthur, C. Jofeh, A.-M. Aguilar, Improving occupant wellness in commercial office buildings through energy conservation retrofits, Buildings 5 (4) (2015) 1171–1186.

[33] B. Thayer, Daylighting and productivity at lockheed, Solar Today 9 (3).

[34] S. Tom, Managing energy and comfort, ASHRAE Journal 50 (6) (2008) 18–27.

[35] C. F. Reinhart, S. Herkel, The simulation of annual daylight illuminance distributions a state-of-the-art comparison of six radiance-based methods, Energy and Buildings 32 (2) (2000) 167 – 187.

[36] J. Mardaljevic, Daylight simulation: validation, sky models and daylight coefficients, Ph.D. thesis, © John Mardaljevic (2000).

[37] N. Igawa, H. Nakamura, All sky model as a standard sky for the simulation of daylit environment, Building and Environment 36 (6) (2001) 763 – 770, building and Environmental Performance Simulation:Current State and Future Issues.

[38] Y. Uetani, S. Aydinli, A. Joukoff, J. Kendrick, R. Kittler, Y. Koga, et al., Spatial distribution of daylight-cie standard general sky, Vienna, Austria.
[39] R. Perez, R. Seals, J. Michalsky, All-weather model for sky luminance distributionpreliminary configuration and validation, Solar Energy 50 (3) (1993) 235 – 245.
[40] A. H. Fakra, H. Boyer, F. Miranville, D. Bigot, A simple evaluation of global and diffuse luminous efficacy for all sky conditions in tropical and humid climate, Renewable Energy 36 (1) (2011) 298–306.
[41] CIE, Standard, Spatial distribution of daylight-cie stndard general sky, CIE S 011.1/E.
[42] C. E. Shannon, Communication in the presence of noise, Proceedings of the IRE 37 (1) (1949) 10–21.
[43] M. Inanici, Evalution of high dynamic range image-based sky models in lighting simulation, The Journal of the Illuminating Engineering Society of North America 7 (2) (2010) 69–84.
[44] G. C. Holst, T. S. Lomheim, CMOS/CCD sensors and camera systems, Vol. 408, JCD publishing USA, 2007.
[45] S. Borkar, A. A. Chien, The future of microprocessors, Communications of the ACM 54 (5) (2011) 67–77.
[46] J. Stumpfel, C. Tchou, A. Jones, T. Hawkins, A. Wenger, P. Debevec, Direct hdr capture of the sun and sky, in: Proceedings of the 3rd international conference on Computer graphics, virtual reality, visualisation and interaction in Africa, ACM, 2004, pp. 145–149.
[47] D. Wüller, H. Gabele, The usage of digital cameras as luminance meters., in: Digital Photography, 2007, p. 65020U.
[48] M. Moeck, S. Anaokar, Illuminance analysis from high dynamic range images, Leukos 2 (3) (2006) 211–228.
[49] A. Borisuit, M. Münch, L. Deschamps, J. Kämpf, J.-L. Scartezzini, A new device for dynamic luminance mapping and glare risk assessment in buildings, in: Proc. of SPIE Vol, Vol. 8485, 2012, pp. 84850M–1.
[50] S. A. Green, D. J. Paddon, Exploiting coherence for multiprocessor ray tracing, IEEE Computer Graphics and Applications 9 (6) (1989) 12–26.
[51] T. Perhavec, A. Gorkič, D. Bračun, J. Diaci, A method for rapid measurement of laser ablation rate of hard dental tissue, Optics & Laser Technology 41 (4) (2009) 397–402.
[52] R. S. Reyes, C. M. Oppus, J. C. N. Monje, N. S. Patron, R. C. Guerrero, J. T. B. Fajardo, Fpga implementation of a telecommunications trainer system, International Journal of Circuits, Systems and Signal Processing 2 (2) (2008) 174–180.
[53] P. J. Pingree, J.-F. L. Blavier, G. C. Toon, D. L. Bekker, An fpga/soc approach to on-board data processing enabling new mars science with smart payloads, in: Aerospace Conference, 2007 IEEE, IEEE, 2007, pp. 1–12.
[54] A. D. Broadbent, A critical review of the development of the cie1931 rgb color-matching functions, Color Research & Application 29 (4) (2004) 267–272.
[55] T. Poikonen, P. Kärhä, P. Manninen, F. Manoocheri, E. Ikonen, Uncertainty analysis of photometer quality factor, Metrologia 46 (1) (2008) 75.
[56] Comission Internationale de l'Eclairage, Methods of characterizing illuminance meters and luminance meters: Performance, characteristics and specifications, Publication CIE (1987) 69–1987.
[57] DIN 5032 part 7, Lichtmessung-klasseneinteilung von beleuchtusstrkeund leuchtdichtemessgerten [photometry: classification of illuminance meters and luminance meters, Deutsches Institut fr Normung e.V. (Dec 1985).
[58] D. B. Goldman, J.-H. Chen, Vignette and exposure calibration and compensation, in: Computer Vision, 2005. ICCV 2005. Tenth IEEE International Conference on, Vol. 1, IEEE, 2005, pp. 899–906.
[59] C. F. Reinhart, S. Herkel, The simulation of annual daylight illuminance distributions a state-of-the-art comparison of six radiance-based methods, Energy and Buildings 32 (2) (2000) 167 – 187.
[60] G. W. Larson, R. Shakespeare, Rendering with Radiance: the art and science of lighting visualization, Booksurge Llc, 2004.
[61] P. R. Tregenza, Subdivision of the sky hemisphere for luminance measurements, Lighting Research & Technology 19 (1) (1987) 13–14.
[62] Y. Wu, J. H. Këmpf, J.-L. Scartezzini, Characterization of a quasi-real-time lighting computing system based on hdr imaging, Energy Procedia 122 (2017) 649–654.
[63] S. Darula, R. Kittler, C. A. Gueymard, Reference luminous solar constant and solar luminance for illuminance calculations, Solar Energy 79 (5) (2005) 559–565.
[64] R. Szeliski, Computer vision: algorithms and applications, Springer Science & Business Media, 2010.
[65] D. L. DiLaura, K. W. Houser, R. G. Mistrick, G. R. Steffy, The lighting handbook: Reference and application, Illuminating Engineering Society of North America New York (NY), 2011.
[66] A. McNeil, The five-phase method for simulating complex fenestration with radiance, 2013.

- A novel embedded photometric device for real-time daylighting simulation.
- High dynamic range (HDR) sky luminance monitoring approach.
- Wide luminance detection range including that of the sun orb, sky, and landscape.
- Calibration of the imaging system in spectral response with f'1 error 8.89%.
- Experimental validation in its improved accuracy of daylighting simulation.